Earth Systems, Resources, and Sustainability, 2026, 1(1), 97–109

Earth Systems, Resources, and Sustainability

Journal Homepage: https://www.sciltp.com/journals/esrs

Article

Nanocrystalline Cookeite from Lithium Mineral Deposits of Jammu, India: A Multianalytical Characterization

Bhaskar J. Saikia[1,*], G. Parthasarathy[2,3], Binoy K. Saikia[4], Puja Bordoloi[4], Rashmi R. Borah[5], Pankaj K. Srivastava[6] and Manavalan Satyanarayanan[7]

[1] Department of Physics, Anandaram Dhekial Phookan College, Nagaon 782002, India
[2] School of Natural and Engineering Sciences, National Institute of Advanced Studies, Indian Institute of Science Campus, Bengaluru 560012, India
[3] DAE-Raja Ramanna Chair Professor, Atomic Minerals Directorate for Exploration & Research (AMD), Naagarabhaavi, Bengaluru 560072, India
[4] Coal and Energy Group, CSIR-North East Institute of Science and Technology, Jorhat 785006, India
[5] Department of Physics, Nagaon University, Nagaon 782001, India
[6] Department of Geology, University of Jammu, Jammu 180006, India
[7] Geochemistry Division, CSIR-National Geophysical Research Institute, Hyderabad 500007, India
[*] Correspondence: vaskaradp@gmail.com

ABSTRACT

This study presents the first integrated micro-Raman spectroscopic and nanoscale investigation of the lithium-bearing bauxite from the Reasi inlier in Jammu. Combined XRD, Raman, FTIR, and high-resolution TEM analyses reveal a mineral assemblage dominated by kaolinite and Li-rich chlorite-group minerals (cookeite), with minor carbonaceous and oxide phases. Powder XRD pattern indicates nanocrystalline intergrowths and mixed-layer domains. Micro-Raman spectra exhibit characteristic Al–O–Si bending and Si–O stretching vibrations diagnostic of kaolinite and cookeite, while FTIR spectra show distinct Si–O and Al–OH bands with broadened Li–O lattice features. HRTEM imaging reveals alternating nanocrystalline and amorphous regions, consistent with partial amorphization and structural reorganization. Energy Dispersive Spectra (EDS) data confirm enrichment of Al, Si, O, and minor Fe, supporting an aluminosilicate framework. These results suggest that kaolinite and cookeite formed through hydrothermal alterations and secondary phyllosilicate formation as a weathering product. Our study contributes to the distribution of lithium minerals which critical for both resource characterization and the development of effective processing strategies.

ARTICLE INFO

History:

Received 14 November 2025
Revised 17 December 2025
Accepted 22 December 2025
Published: 26 December 2025

Keywords:

lithium;
cookeite;
kaolinite;
Raman;
FTIR;
HRTEM

Citation:

Saikia, B.J.; Parthasarathy, G.; Saikia, B.K.; et al. Nanocrystalline Cookeite from Lithium Mineral Deposits of Jammu, India: A Multianalytical Characterization. *Earth Systems, Resources, and Sustainability* **2026**, *1*(1), 97–109. https://doi.org/10.53941/esrs.2026.100006

Copyright: © 2025 by the authors. This is an open access article under the terms and conditions of the Creative Commons Attribution (CC BY) license (https://creativecommons.org/licenses/by/4.0/).
Publisher's Note: Scilight stays neutral with regard to jurisdictional claims in published maps and institutional affiliations.

Research Highlights

- Integrated micro-Raman spectroscopic and nanoscale investigation of the Jammu lithium-bearing bauxite.
- Micro-Raman spectra exhibit characteristic Al–O–Si bending and Si–O stretching vibrations diagnostic of kaolinite and cookeite.
- Kaolinite and cookeite formed through hydrothermal alteration.

1. Introduction

Lithium is a critical element for the manufacture of rechargeable batteries and plays a pivotal role in the global transition toward sustainable energy systems and green transportation [1, 2]. The growing global demand for lithium highlights the need to expand known resources and identify new exploration targets. Lithium deposits occur in three principal geological settings: pegmatites, brines, and volcano-sedimentary deposits [3–7]. A subset of volcano-sedimentary lithium deposits comprises bauxitic deposits, which typically develop in karstic environments and contain Li-bearing minerals such as cookeite, smectite, kaolinite, and illite. Cookeite, a Li-rich member of the chlorite group with the ideal formula $LiAl_4(Si_3Al)O_{10}(OH)_8$ [8], commonly forms as a late-stage hydrothermal alteration product of spodumene, petalite, and other Li-bearing silicates in granitic pegmatites under low-temperature conditions [9–13]. It is occasionally reported from hydrothermal veins and altered sedimentary sequences [14]. Cookeite has also been identified in crystal-rich inclusions associated with granitic pegmatites [15], where its occurrence signifies late hydrothermal overprinting. Consequently, the presence of cookeite in crystal-rich inclusions is generally interpreted as evidence for secondary, post-magmatic fluid activity [16–21].

Bauxitic deposits of the Jammu region commonly contain Li-bearing minerals, including cookeite, smectite, kaolinite, and illite. Lithium extraction and mineralogical characterization from these deposits are challenging due to their complex formation environments and the coexistence of multiple clay minerals. In addition, the extremely fine-grained, often nanocrystalline nature of Li-bearing phases, coupled with the low atomic number of lithium, limits the effectiveness and resolution of conventional analytical techniques such as XRF in accurately estimating lithium contents. Consequently, a clear understanding of the geochemical behaviour and spatial distribution of lithium in these deposits is critical for both resource characterization and the development of effective processing strategies. Bauxitic sedimentary resources containing cookeite have been reported worldwide, with significant occurrences in Europe, India, the USA, and China. In Europe, Li-bearing bauxite deposits are hosted in Cretaceous rocks in Hungary [22], Jurassic–Cretaceous rocks in Greece [23], and Triassic rocks in Italy [24]. In the USA, Late Carboniferous bauxite deposits with lithium concentrations exceeding 2000 ppm have been documented in Missouri and the Pennsylvania–Maryland region [25]. The lithium deposits investigated in this study are located in the Salal-Haimana areas of the Reasi district, Jammu and Kashmir (Figure 1), where Geological Survey of India (GSI, 2022) has reported a 5.9-million-ton lithium resource hosted in bauxite ore, with Li_2O contents reaching up to 0.3%. The specific area of the deposit is generally located between the following coordinates: Latitude: $33°9'40.005''$ N to $33°10'28.104''$ N; Longitude: $74°48'29.224''$ E to $74°49'47.362''$ E. More recently, Wang et al. (2025) highlighted the technical challenges associated with lithium exploration and extraction in their detailed study on the genesis of cookeite, the primary lithium-bearing mineral in the Late Carboniferous strata of the North China Craton [26].

Regional tectonics and stratigraphy play a critical role in controlling the physical and chemical conditions necessary for the formation of cookeite and kaolinite by regulating fluid circulation pathways, temperature–pressure regimes, host rock availability, and the preservation of favorable geochemical environments. Tectonic processes generate fault and fracture networks that act as effective conduits for fluid migration, facilitating the circulation of Li-rich, low-temperature ($<200\,°C$) hydrothermal fluids that promote the formation of cookeite as a late-stage alteration product of lithium-bearing minerals, while kaolinite may also develop through similar hydrothermal processes. The formation of cookeite is strongly dependent on the presence of Li-rich source rocks, such as pegmatites containing lepidolite and spodumene, within the local stratigraphic framework. In the present study area, these interacting processes indicate a complex genetic history in which lithium becomes incorporated into the evolving bauxite matrix, ultimately forming a significant resource, with Li^+ ions substituting for Mg and Fe in the crystal structures of clay minerals (kaolinite, illite) and iron–manganese oxides; although kaolinite is the primary lithium-bearing mineral in bauxite, cookeite can host substantial lithium contents where both minerals coexist.

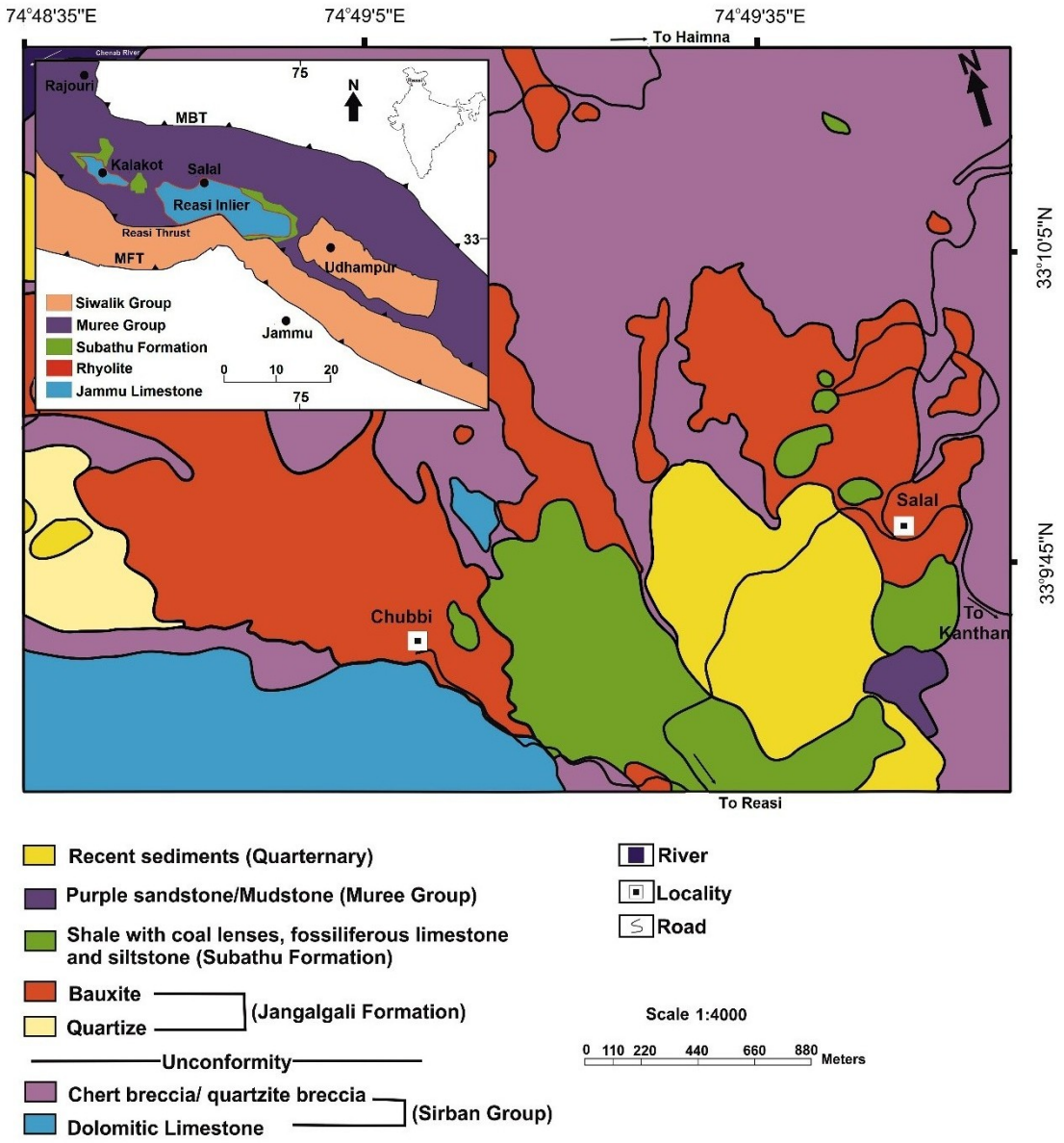

Figure 1. Geological map of the Salal area (modified after Sharma et al., 2025) [27]. The inset map is showing Reasi Inlier in the geological map of Jammu region (after Acharya and Saha, 2018) [28].

To date, no characteristic Raman spectrum of cookeite has been documented. The absence of well-defined Raman signatures in the RRUFF database and other spectroscopic references [29] highlights the analytical challenges in identifying cookeite through vibrational spectroscopy, suggesting that structural disorder, fine crystallinity, and compositional variability within the mineral hamper the development of distinct vibrational bands. This spectral uncertainty complicates the identification of cookeite by Raman spectroscopy alone and necessitates the integration of complementary techniques such as FTIR, XRD, and TEM for confident phase discrimination. In this context, the Jammu sample provides a rare case where combined Raman, FTIR, and high-resolution TEM analyses reveal spectral and structural attributes consistent with Li-rich chlorite-group phases, enabling the spectroscopic characterization of natural cookeite intergrown with kaolinite. It is difficult to characterise lithium unambiguously because of low X ray scattering factor. Lithium is usually estimated by using ICPMS technique [2].

To the best of our knowledge, there are no previous reports on cookeite using micro-Raman spectroscopic or infrared spectroscopic investigations on the Jammu lithium-bearing bauxite from the Reasi area, India. Sharma et al. (2025) provided a comprehensive account of the study area and lithium distribution [27]. However, their study did not include spectroscopic analyses, which are essential for the definitive identification and characterization of rare minerals such as cookeite. Spectroscopic techniques are particularly powerful for the characterization of rare minerals such as cookeite. Earlier studies did not report cookeite in their XRD results because it occurs in a nanocrystalline

form, which is often difficult to detect using conventional XRD methods. The present study addresses this limitation by employing FTIR and micro-Raman spectroscopy, which are highly effective tools for identifying and characterizing nanocrystalline phases [30]. In the present study, we report, for the first time, the detailed spectroscopic investigations to characterize Jammu lithium-bearing bauxite from the Reasi inlier, India using Raman and Fourier-transform infrared (FTIR) spectroscopy with complementary support from high-resolution Transmission Electron Microscopy (HR-TEM), Energy-Dispersive Spectroscopy (EDS), and X-ray diffraction (XRD).

1.1. Geological Settings

Geologically, Reasi area occupies a transitional belt where Precambrian inliers are surrounded by younger Tertiary sedimentary sequences of the Sub-Himalaya (Subathu–Murree–Siwalik succession). The Reasi Inlier with its exposed length of 40 km and breath varying between 8 to 20 km, is the largest out of four inliers present in the area. It consists of thick Precambrian carbonate sequence. One of the defining structural features in Reasi is the Main Boundary Fault (MBF), locally termed the Reasi Thrust (Figure 1). This major fault forms a tectonic boundary between Lower Himalayas and the Precambrian outcrops of Sirban Limestone. Intense Himalayan tectonism has folded the Sirban Limestone into a sequence of anticlines, domes, and localized synclinal troughs.

The geological framework of the area was first described by Medlicott (1876) and later refined by subsequent studies [31–34]. The carbonate succession is collectively termed the Sirban Group, which has been assigned a Proterozoic age based on stromatolite and microorganism evidence [35, 36]. The Sirban Group is unconformably overlain by the Tertiary Jangalgali and Subathu formations. The Sirban Group is subdivided into two formations, namely the Trikuta and Khairikot formations [34]. The Trikuta Formation consists of a predominantly calcareous sequence comprising cherty and non-cherty dolomite, calc-argillite, calc-arenite, slate, flaggy limestone, and stromatolitic limestone/dolomite. The Khairikot Formation is dominated by areno-argillaceous rocks, chiefly quartzite, slate, and variegated shales, with a single stromatolite-bearing dolomite band.

The Jangalgali Formation is unconformably overlying the Khairikote Formation and at places, it is directly overlying the Trikuta Formation, if the latter is missing. The contact is marked with the presence of chert quartzite breccia followed by thin bedded quartzite and thick bauxite. The Jangalgali Formation was earlier referred as the “Bauxite Series” by Middlemiss (1929). The formation consist of gray to brownish coloured chert quartzite breccia at bottom followed by thin linear layers of ferruginous sandy shale. The Upper part of the Jangalgali Formation consist of thick Bauxite column exposed at Muttal to Jangalgali. It is however well developed at Salal (Figure 1).

In the present area of study, Salal ($33°10'$ N: $74°50'$ E), the lithium rich bauxite rests over the chert quartzite breccia. The thickness of bauxite beds varies from 1.5 m to 9 m. The bauxite present in the area can be petrographically divided into three groups. The pisolitic layer occurs at the top and the kaolinite at the bottom, with semi- to non-pisolitic material in between. The upper layer consists of closely packed spherical to flattened pisolites, 2 mm to 1 cm in diameter.

Banerjee (1975) suggested that the flattening of pisolites resulted from Himalayan orogenic movements [37]. The semi- to non-pisolitic layer is hard and contains occasional small gray pisolites. The aluminous clay forms the basal part of the bauxite profile and is yellowish to brownish gray in color. These bauxites are interpreted to have formed by *in situ* residual weathering of shales and clays deposited in local depressions over the Precambrian basement, with bauxitization controlled by leaching intensity and local drainage conditions [38]. Kalsotra (1992) has reported high volumes of Lithium based on the trace elements study of Jammu bauxite [39]. Siddaiah and Shukla (2012) reported presence of the rhyolite at Kalakaot, Beragua, and Khargala [40]. The rocks of Jangalgali Formation are overlain by rocks of Subathu Formation (Carbonaceous shale with coal lenses and Fe- nodules, khaki shale with persistent bands of Nummulitic limestone) of Palaeocene–Eocene Age. The contact between the Jangalgali Formation and the carbonaceous shale of the Subathu Formation is sharp and clearly visible.

2. Experimental

Structural characterization of the Jammu lithium-bearing sample was performed using a high-resolution transmission electron microscope (HR-TEM; JEM-2100 Plus, JEOL Co., Ltd., Japan) operated at an accelerating voltage of 200 kV. For HR-TEM analysis, a few milligrams of the sample were dispersed in isopropyl alcohol and ultrasonicated for 7–8 h to obtain a uniform suspension. Subsequently, 2–3 μL of the dispersion was drop-cast onto a copper TEM grid using a 10 μL micropipette. The grid was placed on a clean Petri dish cover cushioned with tissue paper to prevent contamination. The sample was air-dried for a few minutes and then kept overnight in a vacuum desiccator to ensure complete solvent evaporation. The dried grid was analyzed the following day. Selected-area electron diffraction (SAED) patterns were recorded to examine crystallographic orientations and microstructural features, and nanoscale chemical compositions were determined using an Oxford Instruments energy-dispersive X-ray spectroscopy (EDS) detector attached to the TEM [41].

A fraction of the powdered sample was analyzed by X-ray diffraction (XRD) using a Philips PW 3710/31 diffractometer (Philips, USA) equipped with a scintillation counter, CuKα radiation ($\lambda = 1.54184$ Å), and a Ni filter operated at 40 kV and 35 mA. Data were collected at room temperature over the 2θ range of $10°$–$80°$ in step-scan mode, with a step width of $0.02°$ and a counting time of 5 s per step. The instrument was configured with a divergence slit of 0.5 mm and a receiving slit of 0.3 mm. Mineral phase

identification was carried out by comparison with standard reference patterns at ambient conditions from the RRUFF database (http://rruff.info/) (accessed 1 October 2025).

Raman spectroscopic analyses is conducted on bulk powdered samples of Jammu using a Jobin-Yvon Horiba LabRam-HR Micro-Raman spectrometer (Horiba Scientific, USA) equipped with an Olympus optical microscope and 10×, 50×, and 100× objectives. A Nd:YAG laser (532 nm, ∼5 mW) served as the excitation source. Powdered samples were preferred over polished thin sections to minimize textural and crystallite orientation effects, providing more reliable characterization of mineral phases in both Raman and powder XRD analyses [41]. The system included a motorized x–y stage and an 1800 grooves mm^{-1} grating, covering 100–3000 cm^{-1}. Spectra were calibrated using a silicon wafer (520.7 ± 0.5 cm^{-1}). The instrument offers excellent accuracy (± 0.5 cm^{-1}) and precision (± 0.1 cm^{-1}), facilitating unambiguous mineral identification. An edge filter isolated Stokes lines, and spectra were acquired at room temperature (∼30 °C) with counting times of 10–60 s, depending on fluorescence and signal intensity. Data were processed via baseline correction and Gaussian fitting, and phase identification was achieved by comparison with reference spectra from the RRUFF database (http://rruff.info/).

Powdered samples were homogenized with spectrophotometric grade KBr (1:20) in an agate mortar and pressed into 3 mm pellets using a manual press. Grinding time was minimized to limit lattice distortion, cation exchange, and atmospheric moisture uptake. Infrared spectra were acquired on a PerkinElmer System 2000 FTIR spectrometer (PerkinElmer, USA) with a helium–neon laser reference, operating at a resolution of 4 cm^{-1}. Measurements were performed in transmission mode over the 400–4000 cm^{-1} range at room temperature (29 °C). Particular emphasis was placed on the 400–1200 cm^{-1} region, which record Si–O stretching and bending modes in SiO_4 tetrahedra and provides constraints on silicate polymerization and structural organization.

3. Results and Discussion

The nanoscale structural morphology of the Jammu lithium bearing sample (Figure 2a–f) reveals aggregated sheet-like domains with flake-like morphology at low magnification (200 nm), consistent with carbonaceous–silicate intergrowths. With increasing magnification (100–50 nm), these sheets show semi-transparent, wrinkled textures indicative of turbostratic disorder and shock-induced deformation. At higher resolutions (20–10 nm), lattice fringes within amorphous zones reflect partial crystallinity. At highest resolution (5 nm), well-resolved fringes confirm nanocrystalline particles embedded in an amorphous matrix. The coexistence of crystalline and amorphous domains indicates partial amorphization, reorganization of carbonaceous matter, and impact-related metamorphic reworking in the Jammu sample.

We observe large-aggregated sheet like structures with flake like morphology at 200 nm (Figure 2a). As there is an increase in magnifications, specifically at 100 nm and 50 nm (Figure 2b,c), these sheets display a semi-transparent and wrinkled nature. At higher resolutions, the appearance of lattice fringes reveals partial crystallinity within the nanosized amorphous domains (Figure 2d,e). The distinct crystalline lattice fringes observed at 5 nm (Figure 2f), confirms, well-ordered nanocrystals embedded within an amorphous matrix. These observations collectively indicate a composite structure of disordered carbonaceous matter and nanocrystalline phases.

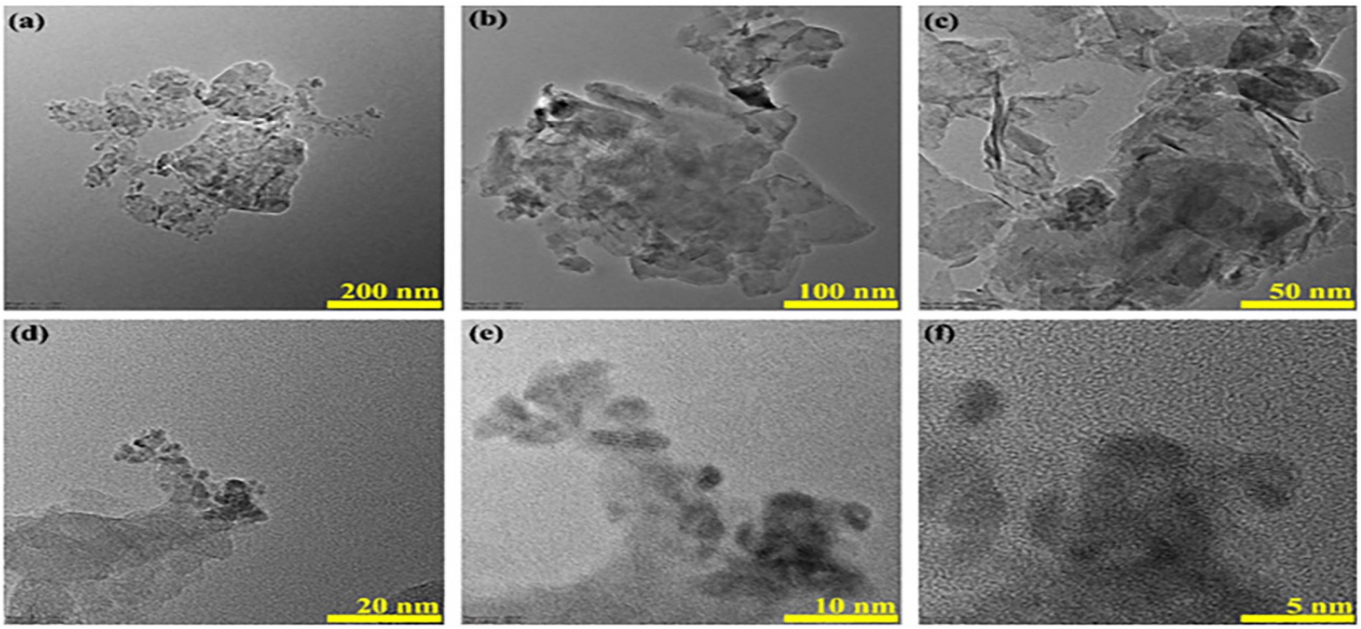

Figure 2. (**a**–**f**) Structural morphology of Jammu lithium bearing sample at magnifications ranging from 200–5 nm.

The EDS analysis of the Jammu sample confirms the presence of oxygen (38.06 wt%), aluminium (22.00 wt%), silicon (18.90 wt%), carbon (18.26 wt%), and minor iron (2.77 wt%). The high O and C contents support the coexistence of carbonaceous matter with oxide/silicate phases [42, 43]. Elevated Al and Si concentrations are consistent with aluminosilicate frameworks, suggesting phases such as phyllosilicates, or feldspathoid-like structures [44]. The low Fe content indicates limited metallic or sulfide inclusions, reflecting either primary mineralogy or subsequent weathering/alteration processes.

Characteristic *d*-spacings, serving as structural fingerprints, were measured in the Jammu sample over a 10 nm scale from lattice-fringe regions using ImageJ software and compared with standard reference values for phase identification. Nanocrystalline domains with distinct lattice fringes are observed, with measured interplanar spacings of 4.26, 3.84, 3.64, 3.02, and 2.6 Å (Figure 3a). These spacings suggest the presence of multiple crystalline phases, including phyllosilicates, aluminosilicates [45], and iron oxides, consistent with EDS data indicating high Si, Al, O, and minor Fe contents [46]. The plausible phase inference that can be predicted from these calculated d-spacings (measured d-space) by referring to the reported phases with respective d-spacings (observed d-space) is listed in Table 1. According to quantitative phase analysis, tourmaline group and chlorite group phases are identified as the principal Li-hosting cookeite. The d-spacings were calculated by dividing the total distance between parallel planes by the number of intensity peaks in the Gray value–distance profile (Figure 3b,c).

The selected area electron diffraction (SAED) pattern (Figure 4a,b) shows *d*-spacings values of $\sim$1.85, 1.18, 0.95, and 0.85 Å. These values correspond to crystallographic planes characteristic of silicates, aluminosilicates, and oxide phases. Together with the EDS results, indicating high O, Al, Si and minor Fe, the data confirm the presence of nanocrystalline aluminosilicates and iron oxides.

The powder X-ray diffraction (XRD) pattern (Figure 5) shows distinct reflections corresponding to both kaolinite and cookeite, confirming a mixed phyllosilicate assemblage.

Sharp kaolinite peaks are accompanied by additional reflections at $\sim$30–32°2θ and 36–$40°2\theta$, characteristic of Li-rich chlorite-group minerals such as cookeite. The partial overlap and broadening of peaks in the 20–40°2θ range indicate nanoscale intergrowths or mixed-layer domains between kaolinite and cookeite. These results, together with spectroscopic data, suggest that kaolinite formed contemporaneously with or as a product of the hydrothermal alteration of cookeite-bearing assemblages.

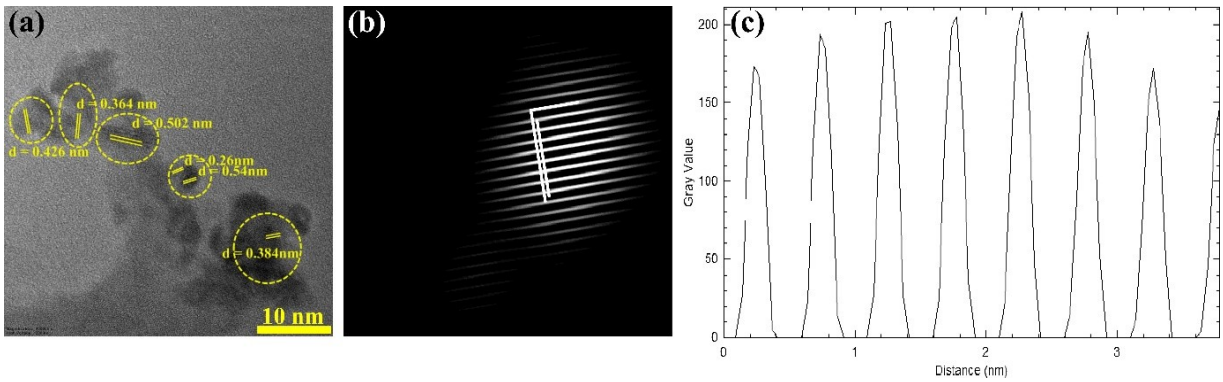

Figure 3. (**a**) d-space at different lattice fringes within 10 nm (**b**) distance between a number of crystal fringes through inverse FFT for evaluation of d-space (**c**) gray value showing the number of peaks.

Table 1. Summary of calculated and reported d-spacing of Li-hosting mineral phases.

Calculated *d*-spacing	Reported *d*-spacing	Phase	References
4.26	4.265	Quartz	Aidid, A.R. et al., 2025 [47]
3.84	3.84	Ordered Kaolinite	García-Vicente, Andrea, et al, 2021 [48]
3.64	3.51	Chlorite group	Wang et al., 2025 [26]
3.02	4.93–5	Tourmaline group	Wang et al., 2025 [26]
2.6	2.7	Hematite (Fe_2O_3)	Chernyshova, I.V. et al, 2013 [49]
1.85	1.78–1.8	Kaolinite	Abass, M.M.R. et al., 2019 [50]

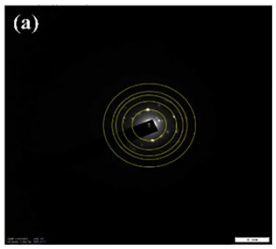

(b)

Major	Minor (1/2r)	1/r=(1/2r/2)	r=1/(1/r)	d-space=r*10	d-space(Å)
10.903	10.797	5.396	0.185322	1.853224611	~1.85
16.968	16.897	8.4485	0.118364	1.183642067	~1.18
21.228	21.047	10.5235	0.095025	0.950254193	~0.95
23.901	23.394	11.697	0.085492	0.854920065	~0.85

Figure 4. (**a**) SAED pattern of Jammu (**b**) calculation of d-space from the rings of SAED pattern.

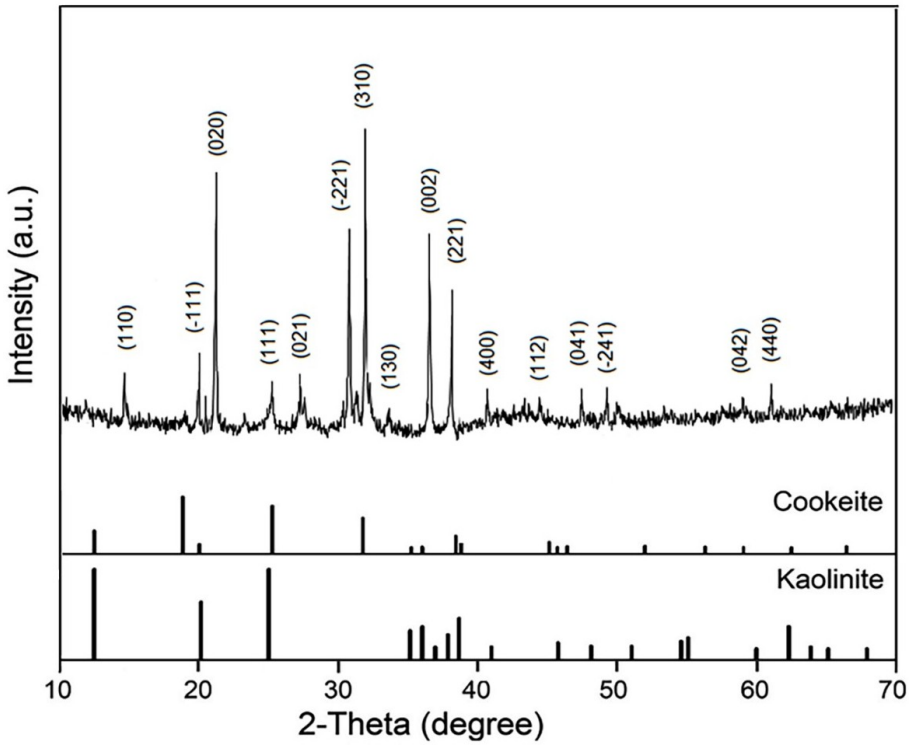

Figure 5. XRD patterns of the Li-rich claystone in the Reasi area, Jammu.

The Raman spectra display distinct bands in the range of 100–1300 cm^{-1}, attributable to nanocrystalline cookeite and certain phases of kaolinite (Figures 6 and 7). These characteristic features correspond to lattice vibrational modes and Al–O/Si–O stretching vibrations, confirming the occurrence of phyllosilicate minerals within the studied samples. Most of the Raman peaks observed in this study are in good agreement with the Raman study of cookite inclusions in Spodemune. In low- to mid-wavenumber region (100–600 cm^{-1}) of the Raman spectra (Figures 6 and 7) display peaks at 167, 219, 266, 341–342, 382, 464, and 592 cm^{-1}, corresponding to nanocrystallized cookeite, typically develops as a secondary phase through hydrothermal alteration of spodumene and other aluminosilicates [51]. In the low-wavenumber region (100–300 cm^{-1}), weaker bands attributable to nanocrystalline cookeite occur near 185, 219, 249, and 295, and 296 cm^{-1}, corresponding to translational and rotational lattice modes involving Li^{+} and Al^{3+} cations [51]. However, Ding et al. (2020) demonstrated that the Raman spectra of the hydrous solid phase are characterized by a series of well-resolved and diagnostic bands at 98, 167, 219, 266, and 3640 cm^{-1} [52]. Raman bands attributable to cookeite occur mainly in the low- to mid-wavenumber regions and may overlap with kaolinite and spodumene features in the nanocrystalline samples. Mid-region bands at ∼266 and 324 cm^{-1} are commonly observed in cookeite and relate to tetrahedral–octahedral coupling and the torsional modes of the SiO_4 tetrahedra associated with nearby Li/Al sites. However, the bands at ∼382 and 464 cm^{-1} occur in both cookeite and kaolinite; in cookeite these reflect Al–O–Si bending and chlorite-type sheet interactions and are typically broader and less sharp than the corresponding kaolinite bands. The peaks near ∼527 and 588–592 cm^{-1} are assigned to combined Si–O–Al bending and M–O stretching (octahedral metal-oxygen) in the chlorite structure. The mid-region band near ∼708–709 cm^{-1} may appear in both cookeite and coexisting phases but in cookeite it is often less intense and

broader than the sharp kaolinite 709 cm^{-1} diagnostic peak. In right-wavenumber region (900–1100 cm^{-1} region), Si–O stretching bands for cookeite are generally weaker or broadened and can be masked by strong spodumene or kaolinite signals (Figure 8). The prominent peaks at 904, 1021, and 1027 cm^{-1} arise from asymmetric stretching of Si–O bonds in both isolated and bridging tetrahedra, while the peak at 1072 cm^{-1} is associated with high-frequency asymmetric stretching modes involving bridging oxygen atoms within the silicate framework.

Moreover, the micro-Raman spectrum of the spodumene–cookeite assemblage (Figure 8) exhibits distinct vibrational bands between 200 and 1200 cm^{-1}, confirming the coexistence of both minerals. This effect arises when analyses are performed on overlapping or closely spaced fine grains, where the laser beam simultaneously excites both phases due to its spot size. In this case, the detector records photons scattered from two distinct minerals, producing a composite spectrum that represents the mathematical sum of their individual signatures [30, 53–56]. Prominent peaks at 300, 356, 398, 524, 708, 1020, 1072, and 1098 cm^{-1} are diagnostic of spodumene and correspond to lattice and Si–O stretching vibrations [57]. Additional bands at approximately 266, 324, 382, 464, 524, 590, and 708 cm^{-1} represent overlapping features of nanocrystalline cookeite and spodumene, suggesting mixed-phase excitation caused by their nanocrystalline intergrowths. The broad peaks indicates that cookeite is nano-crystalline in nature. The occurrence of nanocrystalline cookeite in close association with comparatively more crystalline (Sharp peaks compared to cookeite) spodumene indicates hydrothermal alteration of primary spodumene, during which Li and Al were mobilized and reprecipitated under late-stage, fluid-rich conditions [12, 16–18].

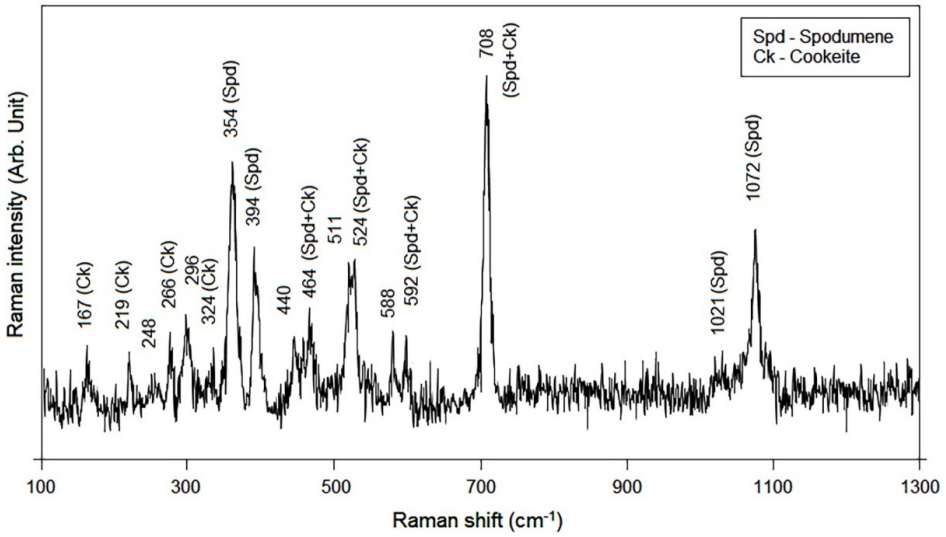

Figure 6. Raman spectrum of the Li-rich claystone in the Reasi area, Jammu in the range 100–1300 cm^{-1}.

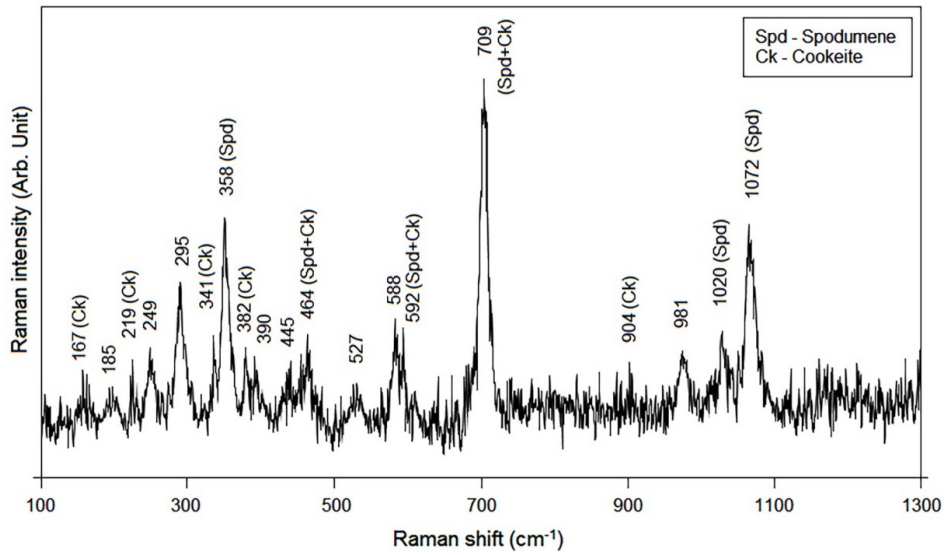

Figure 7. Raman spectrum of the Li-rich claystone in the Reasi area, Jammu in the range 100–1300 cm^{-1}.

The FTIR spectrum (Figure 9) in the 400–1600 cm^{-1} region reveals characteristic absorption bands attributable to the vibrational modes of kaolinite with additional minor contributions from Li-bearing chlorite-group phase, unambiguously interpreted as cookeite. The intense absorptions between 1140 and 1018 cm^{-1} (1140, 1084, 1066, and 1018 cm^{-1}) correspond to Si–O stretching and Si–O–Al asymmetric stretching vibrations of tetrahedral silicate sheets, typical of well-ordered kaolinite. These modes arise from the internal vibrations of the SiO4 tetrahedra and are diagnostic of the structural integrity of the 1:1 layer silicate framework [58]. The band at 916 cm^{-1} is attributed to the Al–Al–OH deformation mode, a distinctive feature of kaolinite reflecting hydroxyl groups coordinated to octahedral Al^{3+} cations.

The weaker band at 858 cm^{-1} is assigned to Al–OH vibrational or bending modes involving octahedral sheet vibrations, while the broad composite bands at 636 and 582 cm^{-1} correspond to coupled Si–O–Al bending and metal–oxygen lattice deformation vibrations within the tetrahedral–octahedral framework. The peaks observed at 527 cm^{-1} and 463–447 cm^{-1} are related to Al–O–Si deformation and M–O (metal–oxygen) stretching modes, respectively, and indicate the presence of octahedral coordination typical of kaolinite and chlorite structures.

The spectrum is dominated by kaolinite, but the broadened Si–O stretching bands (1084–1018 cm^{-1}) and increased absorption in the 500–650 cm^{-1} region reveal minor overlapping contributions from cookeite. In cookeite, the Li–O and Al–O lattice vibrational modes are typically observed in the 500–650 cm^{-1} region, while the Si–O–Al stretching vibrations occur as broad and relatively weak features between 1080 and 1010 cm^{-1}, reflecting the structural disorder of the Li-bearing chlorite framework. These overlapping bands result in a composite spectral signature, in which the sharp Si–O stretching features of kaolinite become partially broadened due to structural disorder and vibrational coupling introduced by mixed-layer domains or nanocrystalline cookeite.

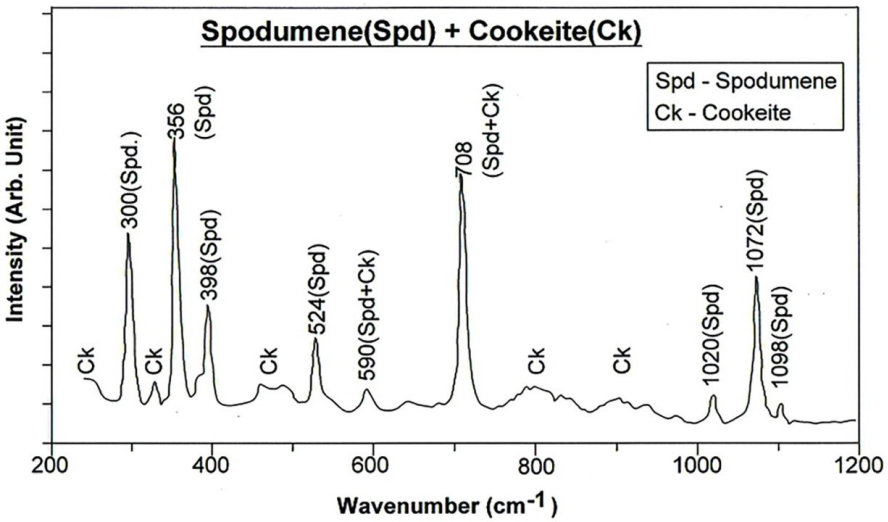

Figure 8. Micro-Raman spectrum of the Li-rich claystone in the Reasi area, Jammu in the range 200–1200 cm^{-1} exhibit the combined phase of spodumene and cookeite.

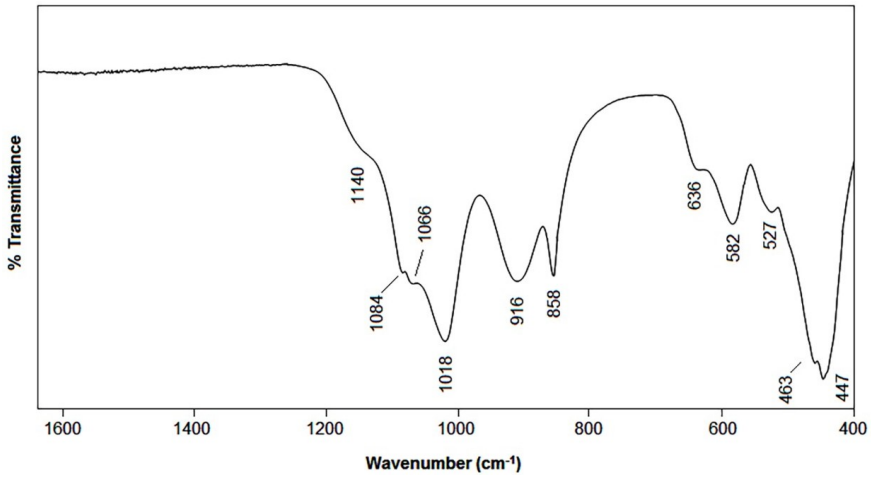

Figure 9. Mid infrared spectrum of the Li-rich claystone in the Reasi area, Jammu in the range 400–1600 cm^{-1}.

This interpretation is consistent with the Raman spectral data, where low-wavenumber lattice modes at 185–249 cm^{-1} and mid-range vibrations near 527–588 cm^{-1} are indicative of cookeite intergrowths with kaolinite. The coexistence of both minerals supports a hydrothermal alteration sequence, where primary aluminosilicate phases underwent Li- and Al-mobilization leading to the formation of cookeite–kaolinite assemblages.

The FTIR spectrum in the 3200–3600 cm^{-1} region (Figure 10) reveals multiple well-defined OH-stretching absorptions characteristic of kaolinite, together with additional broad features indicative of Li-bearing chlorite-group (cookeite) contributions. Kaolinite typically exhibits four sharp and diagnostic OH-stretching bands at approximately 3620, 3650, 3668, and 3695 cm^{-1}, corresponding respectively to inner-surface and inner hydroxyl groups involved in hydrogen bonding between adjacent layers [58–60]. In the present spectrum, these kaolinite-related modes appear as strong to moderate features centered at 3520 and 3570 cm^{-1}, but show slight broadening and reduced resolution relative to pure kaolinite, reflecting partial structural disorder and the influence of interlayer hydration.

Additional broad absorptions peaks at 3410–3445 cm^{-1} and a weaker shoulder near 3315 cm^{-1} correspond to interlayer or adsorbed molecular water vibrations and structurally bound hydroxyls associated with cookeite. Li–Al chlorites such as cookeite display broad composite OH-stretching bands between 3350 and 3470 cm^{-1}, reflecting hydroxyls coordinated to both Li^{+} and Al^{3+} cations [26]. The two broad absorption bands at 3532–3516 and 3355–3335 cm^{-1} in the high-frequency region provide strong evidence for the presence of cookeite within the Li-rich domains, corresponding to OH-stretching vibrations associated with Li–Al octahedral coordination [26]. The overlapping of these bands with kaolinite inner-surface OH absorptions produces a composite structure, where the sharp kaolinite peaks are superimposed upon a broad hydrogen-bonded background typical of chlorite-type phases. The 3420–3445 cm^{-1} band in cookeite is attributed to interlayer water or weakly bound hydroxyls based on its low-frequency position and broad shape. Strongly hydrogen-bonded OH groups, including interlayer or adsorbed water, typically produce broad absorptions near ∼3400 cm^{-1}. In Li–Al chlorites like cookeite, weak OH coordination to Li^{+}–Al^{3+} octahedra or residual interlayer water produces bands in the 3350–3450 cm^{-1} range [26], in contrast to the sharp OH-stretching bands above 3600 cm^{-1} characteristic of well-ordered kaolinite [58]. This spectral behavior supports the interpretation derived from the mid-infrared region and Raman data, indicating mixed-layer kaolinite–cookeite assemblages formed during late-stage hydrothermal reactions.

4. Conclusions

Integrated Raman, FTIR, XRD, and TEM analyses reveal that the Jammu lithium-bearing sample consists predominantly of nanocrystalline kaolinite intergrown with Li-rich chlorite-group minerals (cookeite) within a partially amorphous matrix. XRD patterns show overlapping reflections, indicating mixed-layer kaolinite–cookeite domains, confirming a mixed-layer phyllosilicate system. The broadening and partial overlap of reflections suggests nanocrystalline intergrowths and structural disorder. Raman spectra exhibit diagnostic bands at 167–592 cm^{-1}, attributed to Al–O–Si bending and Si–O stretching modes of cookeite and kaolinite. The overlapping peaks at ∼382, 464, and 590 cm^{-1} indicate mixed-phase excitation between these minerals, while minor spodumene-related bands imply residual precursor phases. FTIR spectra further authenticate this association, showing strong Si–O stretching vibrations at 1140–1018 cm^{-1} and Al–OH deformation near 916 cm^{-1}, typical of kaolinite, with broadened features between 500–650 cm^{-1} reflecting Li–O and Al–O vibrations from cookeite. HRTEM imaging reveals sheet-like nanostructures and alternating nanocrystalline–amorphous domains, supported by SAED patterns showing discrete d-spacings consistent with phyllosilicate and oxide phases. EDS confirms enrichment in Al, Si, O, and minor Fe, consistent with aluminosilicate–oxide intergrowths. Together, these results provide new insights into the nanocrystalline mineralogical processes governing lithium redistribution in pegmatitic systems, highlighting that kaolinite and cookeite formed through hydrothermal alteration during the genesis of Li-bearing phyllosilicate assemblages.

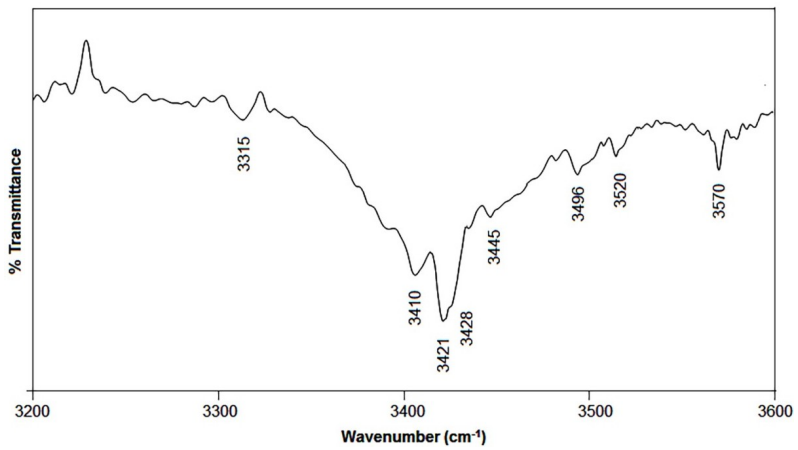

Figure 10. Mid infrared spectrum of the Li-rich claystone in the Reasi area, Jammu in the range 3200–3600 cm^{-1}.

Author Contributions

B.J.S.: Conceptualization; Data curation; Investigation; Visualization; Validation, Writing—original draft, Writing—review & editing. G.P.: Conceptualization; Visualization; Investigation; Supervision; Validation; Writing—review & editing. B.K.S.: Investigation, Data curation, Writing—review & editing. P.B.: Investigation, Data curation. R.R.B.: Investigation, Data curation, Writing—review & editing. P.K.S.: Data curation. M.S.: Data curation. All authors have read and agreed to the published version of the manuscript.

Funding

This research received no external funding.

Institutional Review Board Statement

Not applicable.

Informed Consent Statement

Not applicable.

Data Availability Statement

All data reviewed in this work are presented in the respective articles containing the public archive information.

Acknowledgements

We are grateful to the anonymous Reviewers for very constructive and useful comments which have improved the manuscript. We are grateful to M. Santosh for his kind encouragement and support. The authors thank B. Sreenivas CSIR NGRI for useful discussion. We thank Directors, Indian Institute of Technology, Guwahati (IITG) and North East Institute of Science and Technology (CSIR-NEIST) for providing experimental facilities for characterization of the samples. We also thank S. Sarmah, IIT Guwahati for his assistance in the infrared, micro-Raman spectroscopic and XRD analysis. G.P. is grateful to Department of Atomic Energy, Government of India for supporting under DAE-Raja Ramanna Chair Scheme.

Conflicts of Interest

The authors declare that they have no known competing financial interests or personal relationships that could have appeared to influence the work reported in this paper.

Use of AI and AI-assisted Technologies

During the preparation of this work, the authors used Grammarly English correction Tool. After that, the authors reviewed and edited the content as needed and take full responsibility for the content of the publication.

References

1. Gielen, D. *Critical Minerals for the Energy Transition*; International Renewable Energy Agency: Abu Dhabi, UAE, 2021.
2. Balaram, V.; Santosh, M.; Satyanarayanan, M.; et al. Lithium: A review of applications, occurrence, exploration, extraction, recycling, analysis, and environmental impact. *Geosci. Front.* **2024**, *15*, 101868. https://doi.org/10.1016/j.gsf.2024.101868
3. Kesler, S.E.; Gruber, P.W.; Medina, P.A.; et al. Global lithium resources: Relative importance of pegmatite, brine and other deposits. *Ore Geol. Rev.* **2012**, *48*, 55–69. https://doi.org/10.1016/j.oregeorev.2012.05.006
4. Gourcerol, B.; Gloaguen, E.; Melleton, J.; et al. Re-Assessing the European lithium resource potential—A review of hard-rock resources and metallogeny. *Ore Geol. Rev.* **2019**, *109*, 494–519. https://doi.org/10.1016/j.oregeorev.2019.04.015
5. Bowey, J.E.; Hofmeister, A.M.; Speck, A.K. Infrared spectra of pyroxenes (crystalline chain silicates) at room temperature. *Mon. Not. R. Astron. Soc.* **2020**, *497*, 3658–3677. https://doi.org/10.48550/arXiv.2007.13557
6. Benson, T.R.; Coble, M.A.; Dilles, J.H. Hydrothermal enrichment of lithium in intracaldera illite-bearing claystones. *Sci. Adv.* **2023**, *9*, eadh8183. https://doi.org/10.1126/sciadv.adh8183
7. Putzolu, F.; Armstrong, R.N.; Benson, T.R.; et al. Volcano-Sedimentary deposits: Overview of an emerging type of lithium resource. *Econ. Geol.* **2025**, *120*, 541–573. https://doi.org/10.5382/econgeo.5135
8. Anthony, J.W.; Bideaux, R.A.; Bladh, K.W.; et al. *Handbook of Mineralogy*; Mineral Data Publishing, Mineralogical Society of America: Tucson, AZ, USA, 1995; Volume 2, p. 159.
9. Černý, P. Compositional variation in cookeite. *Can. Mineral.* **1970**, *10*, 636–647.
10. Heinrich, E.W. Economic geology and mineralogy of petalite and spodumene pegmatites. *Ind. J. Earth Sci.* **1975**, *2*, 18–29.
11. London, D.; Burt, D.M. Alteration of spodumene, montebrasite, and lithiophilite in pegmatites of the white picacho District, Arizona. *Am. Mineral.* **1982**, *67*, 97–113.
12. Bobos, I.; Vieillard, P.; Charoy, B.; et al. Alteration of spodumene to cookeite and its pressure and temperature stability conditions in li-bearing aplite-pegmatites from Northern Portugal. *Clays Clay Miner.* **2007**, *55*, 295–310. https://doi.org/10.1346/CCMN.2007.0550306
13. Novak, M.; Copjakova, R.; Dosbaba, M.; et al. Two paragenetic types of cookeite from the Dolní Bory–Hatě pegmatites, moldanubian zone, Czech Republic: Proximal and distal alteration products of li-bearing sekaninaite. *Can. Mineral.* **2015**, *53*, 1035–1048. https://doi.org/10.3749/canmin.1400090
14. Vidal, O.; Goffé, B. Cookeite $LiAl_4(Si_3Al)O_{10}(OH)_8$: Experimental study and thermodynamical analysis of its compatibility relations in the Li_2O–Al_2O_3–SiO_2–H_2O system. *Contrib. Mineral. Petrol.* **1991**, *108*, 72–81.
15. Roedder, E. Fluid inclusion evidence for immiscibility in magmatic differentiation. *Geochim. Cosmochim. Acta* **1992**, *56*, 5–20.
16. Anderson, A.J.; Clark, A.H.; Gray, S. The occurrence and origin of zabuyelite (Li_2CO_3) in spodumene-hosted fluid inclusions: Implications for the internal evolution of rare-element granitic pegmatites. *Can. Mineral.* **2001**, *39*, 1513–1527. https://doi.org/10.2113/gscanmin.39.6.1513
17. Anderson, A.J.; Maccarron, T. Three-dimensional textural and chemical characterization of polyphase inclusions in spodumene using a dual focused ion beam–scanning electron microscope (FIB–SEM). *Can. Mineral.* **2011**, *49*, 541–553. https://doi.org/10.3749/canmin.49.2.541
18. Anderson, A.J. Are silicate-rich inclusions in spodumene crystallized aliquots of boundary layer melt? *Geofluids* **2013**, *13*, 460–466. https://doi.org/10.1111/gfl.12041
19. Ling, K.Y.; Wen, H.J.; Han, T.; et al. Lithium-rich claystone in pingguo area, guangxi, Southwest China: Precursor kaolinite controls lithium enrichment. *Miner. Deposita* **2023**, *59*, 329–340. https://doi:10.1007/s00126-023-01210-x

20. Wang, Z.S.; Li, Y.; Algeo, T.J.; et al. Critical metal enrichment in upper carboniferous karst bauxite of the North China Craton. *Miner. Deposita* **2023**, *59*, 237–254. https://doi.org/10.1007/s00126-023-01207-6
21. Yuan, D.E.; Wang, X.M.; Yan, D.T.; et al. Nanometer-scale mineralogical analyses of cookeite and implications for Li enrichment: No. 21 coal, Mengjin Mine, western Henan. *Int. J. Coal Geol.* **2024**, *283*, 104445.
22. D'Argenio, B.; Mindszenty, A. Cretaceous bauxites in the tectonic framework of the mediterranean. *Rend. Soc. Geol. Ital.* **1987**, *9*, 257–262.
23. Economou-Eliopoulos, M.; Kanellopoulos, C. Abundance and genetic significance of lithium in karst-type bauxite deposits: A comparative review. *Minerals* **2023**, *13*, 962. https://doi.org/10.3390/min13070962
24. Franceschelli, M.; Puxeddu, M.; Memmi, I. Li-, B-rich rhaetian metabauxite, Tuscany, Italy: Reworking of older bauxites and igneous rocks. *Chem. Geol.* **1998**, *144*, 221–242. https://doi.org/10.1016/S0009-2541(97)00133-2
25. Tourtelot, H.A.; Brenner-Tourtelot, E.F. Lithium: A preliminary survey of its mineral occurrence in flint clay and related rock types in the United States. In *Lithium Needs and Resources*; Pergamon: Oxford, UK, 1978; pp. 263–272. https://doi.org/10.1016/B978-0-08-022733-7.50010-1
26. Wang, R.; Ramanaidou, E.; Kirkland, C.L.; et al. Genesis of cookeite, the primary lithium mineral in the late carboniferous strata of the North China craton. *Ore Geol. Rev.* **2025**, *186*, 106903. https://doi.org/10.1016/j.oregeorev.2025.106903
27. Sharma, R.; Mir, S.A.; Misra, P.S.; et al. Metallogenic environment for lithium mineralisation in bauxite from the Salal–Haimna area, Reasi, North West Himalaya of Jammu–Kashmir, India. *Discov. Geosci.* **2025**, *3*, 124. https://doi.org/10.1007/s44288-025-00240-4
28. Acharya, S.K.; Saha, P. Himalayan paleogene foreland basin: Collision-induced early volcanic history and failed rift initiation. *J. Asian Earth Sci.* **2018**, *162*, 3–12. https://doi.org/10.1016/J.JSEAES.2018.04.031
29. Downs, R.T. The RRUFF project: An integrated study of the chemistry, crystallography, Raman and infrared spectroscopy of minerals. In Proceedings of the 19th General Meeting of the International Mineralogical Association, Kobe, Japan, 23–28 July 2006; pp. 3–13.
30. Saikia, B.J.; Parthasarathy, G.; Borah, R.R. Nanodiamonds and silicate minerals in ordinary chondrites as determined by micro-Raman spectroscopy. *Meteorit. Planet. Sci.* **2017**, *52*, 1146–1154. https://doi.org/10.1111/maps.12850
31. Medlicott, H.B. Note upon the sub-Himalayan series in the Jammu (Jammoo) hills. *Rec. Geol. Surv. India* **1876**, *9*, 49–57.
32. Middlemiss, C.S. *Bauxite Deposits of Jammu Province, Jammu*; Mineral Survey Report; Government of Jammu and Kashmir: Srinagar, India. 1928; p. 60.
33. Raha, P.K.; Shastry, M.V.A. Stromatolites from Jammu limestone, Udhampur district, J & K State, their stratigraphic and palaeogeographic significances. *Himal. Geol.* **1973**, *3*, 135–147.
34. Thappa, B.D.; Shali, A.K. Geology of the sirban limestone inliers in Vaishno Devi, Ramsuh–Kalakote and Dansal–Sawalakot Section, Udhampur, Rajori and Doda District, J & K. *Rec. Geol. Surv. India* **1994**, *126*, 24–25.
35. Raha, P.K.; Candy, K.C.; Balasubrahmanyan, M.N. Geochronology of the Jammu limestone, Udhampur District, J & K State. *J. Geol. Soc. India* **1978**, *19*, 221–223.
36. Venkatachala, B.S.; Kumar, A. Fossil microbiota from Vaishnodevi limestone, Himalayan foothills, Jammu: Age and palaeoenvironmental implications. *J. Geol. Soc. India* **1998**, *52*, 529–536.
37. Banerjee, P.K. A reconnaissance survey of the distribution of some trace elements in Indian Bauxite. *Miner. Deposita* **1975**, *10*, 177–188.
38. Lal, M.; Jamwal, J.S.; Nanda, M.M. Bauxite deposits of Jammu, India. In *Laterisation Processes*; Oxford & IBH Publishing Co.: New Delhi, India, 1981; pp. 190–192.
39. Kalsotra, M.R. Strategic and precious metals in the Jammu Himalaya. *Rec. Geol. Surv. India* **1992**, *12*, 6–9.
40. Siddaiah, N.S.; Shukla, M.K. Occurrence of rhyolite in jngalgali formation, Jammu and Kashmir, Northwest Himalaya, India. *Curr. Sci.* **2012**, *103*, 817–821.
41. Saikia, B.J.; Parthasarathy, G.; Saikia, B.K.; et al. First observation of coexisting crystalline and amorphous mineral phases in the bhawad LL6 Chondrite: Evidence from micro-Raman spectroscopic studies. *Geosci. Front.* **2026**, *17*, 102236. https://doi.org/10.1016/j.gsf.2025.102236
42. Dunham, E.T.; Sheikh, A.; Opara, D.; et al. Calcium–aluminum-rich inclusions in non-carbonaceous chondrites: Abundances, sizes, and mineralogy. *Meteorit. Planet. Sci.* **2023**, *58*, 643–671. https://doi.org/10.1111/maps.13975
43. Baruah, P.; Das, B.K.; Bora, M.; et al. Hydrothermally prepared sugar-derived carbon spheres for all-solid-state symmetric electrochemical capacitors. *Mater. Today Commun.* **2022**, *33*, 104219. https://doi.org/10.1016/j.mtcomm.2022.104219
44. Tomioka, N.; Miyahara, M. High-pressure minerals in shocked meteorites. *Meteorit. Planet. Sci.* **2017**, *52*, 2017–2039. https://doi.org/10.1111/maps.12902
45. Thompson, S.P.; Parker, J.E.; Tang, C.C. The 10 μm band in amorphous $MgSiO_3$: Influence of medium-range structure, defects and thermal processing. *Astron. Astrophys.* **2012**, *545*, A60. https://doi.org/10.1051/0004-6361/201219356
46. Lenhardt, K.R.; Breitzke, H.; Buntkowsky, G.; et al. Synthesis of short-range ordered aluminosilicates at ambient conditions. *Sci. Rep.* **2021**, *11*, 1–13. https://doi.org/10.1038/s41598-021-83643-w
47. Aidid, A.R.; Shishir, M.K.H.; Rahaman, M.A.; et al. Powder x-ray line diffraction pattern profiling of anatase–quartz binary oxide: A crystallographic investigation. *Next Mater.* **2025**, *8*, 100571. https://doi.org/10.1016/j.nxmate.2025.100571
48. García-Vicente, A.; García-González, A.; Lorenzo, A.; et al. Field spectroscopy applied to the kaolinite polytypes identification. *Environ. Sci. Proc.* **2021**, *6*, 16. https://doi.org/10.3390/iecms2021-09353
49. Chernyshova, I.V.; Ponnurangam, S.; Somasundaran, P. Linking interfacial chemistry of CO_2 to surface structures of hydrated metal oxide nanoparticles: Hematite. *Phys. Chem. Chem. Phys.* **2013**, *15*, 6953–6964. https://doi.org/10.1039/C3CP44264K
50. Abass, M.M.R. Increasing the D-spacing of kaolinite to intercalate PMMA/Kaolinite nanocomposites. *IOSR J. Appl. Chem.* **2011**, *3*, 01–14. https://doi.org/10.9790/4861-1103010114
51. Li, J.; Chou, I.-M. Occurrence of metastable cristobalite in spodumene-hosted crystal-rich inclusions from jiajika pegmatite deposit, China. *J. Geochem. Explor.* **2016**, *171*, 29–36. https://doi.org/10.1016/j.gexplo.2015.10.012
52. Ding, X.; Li, J.; Chou, I.-M.; et al. Raman spectroscopic identification of cookeite in the crystal-rich inclusions in spodumene from the jiajika lithium pegmatite deposit, China, and its geological implications. *Eur. J. Mineral.* **2020**, *32*, 67–75. https://doi.org/10.5194/ejm-32-67-2020
53. Saikia, B.J.; Parthasarathy, G.; Borah, R.R. High-Ppressure polymorphs of olivine and silica in kamargaon (L6) chondrite: Laser micro-raman and XRD studies. *J. Earth Syst. Sci.* **2022**, *131*, 38. https://doi.org/10.1007/s12040-021-01803-y
54. Saikia, B.J.; Parthasarathy, G.; Chalapathi Rao, N.V.; et al. High shock pressure metamorphism induced transformations of olivine and feldspar in natun balijan l4 chondrite. *J. Geol. Soc. India* **2022**, *98*, 731–739. https://doi.org/10.1007/s12594-022-2061-7
55. Saikia, B.J.; Basak, S.; Borah, R.R.; et al. Spectroscopic investigations and mineral chemistry of dunite from the sargur supracrustals (3 Ga) greenstone belt. *J. Geol. Soc. India* **2022**, *98*, 1505–1512. https://doi.org/10.1007/s12594-022-2205-9

56. Saikia, B.J.; Parthasarathy, G.; Chalapathi Rao, N.V.; et al. Mineral chemistry of Mahadevpur H4/5 chondrite. *Curr. Sci.* **2024**, *126*, 574–582. https://doi.org/10.18520/cs/v126/i5/574-582

57. Pommier, C.J.S.; Denton, M.B.; Downs, R.T. Raman spectroscopic study of spodumene through the pressure-induced phase change from C2/c to P21/c. *J. Raman Spectrosc.* **2003**, *34*, 769–775. https://doi.org/10.1002/jrs.1051

58. Saikia, B.J.; Parthasarathy, G. FTIR characterization of kaolinite from Assam and Meghalaya, Northeastern India. *J. Mod. Phys.* **2010**, *1*, 206–210. https://doi.org/10.4236/jmp.2010.14031

59. Farmer, V.C. *The Infrared Spectra of Minerals*; Mineralogical Society: London, UK, 1974.

60. Madejová, J.; Komadel, P. Baseline studies of the clay minerals society source clays: Infrared methods. *Clays Clay Miner.* **2001**, *49*, 410–432. https://doi.org/10.1346/CCMN.2001.0490508